

# Cryo-electron microscopy structure of the TRPV2 ion channel

Lejla Zubcevic<sup>1,3</sup>, Mark A Herzik Jr<sup>2,3</sup>, Ben C Chung<sup>1</sup>, Zhirui Liu<sup>1</sup>, Gabriel C Lander<sup>2</sup> & Seok-Yong Lee<sup>1</sup>

**Transient receptor potential vanilloid (TRPV) cation channels are polymodal sensors involved in a variety of physiological processes. TRPV2, a member of the TRPV family, is regulated by temperature, by ligands, such as probenecid and cannabinoids, and by lipids. TRPV2 has been implicated in many biological functions, including somatosensation, osmosensation and innate immunity. Here we present the atomic model of rabbit TRPV2 in its putative desensitized state, as determined by cryo-EM at a nominal resolution of ~4 Å. In the TRPV2 structure, the transmembrane segment 6 (S6), which is involved in gate opening, adopts a conformation different from the one observed in TRPV1. Structural comparisons of TRPV1 and TRPV2 indicate that a rotation of the ankyrin-repeat domain is coupled to pore opening via the TRP domain, and this pore opening can be modulated by rearrangements in the secondary structure of S6.**

Transient receptor potential (TRP) channels are a superfamily of non-selective cation channels that are activated by various physical and chemical stimuli and are involved in diverse cellular processes ranging from neuronal development to sensory transduction<sup>1</sup>. In mammals, six TRP channel families (TRPC, TRPV, TRPM, TRPP, TRPML and TRPA) constitute the TRP channel superfamily. Four TRPV family members, TRPV1–TRPV4, have been implicated in thermal sensation characterized by different temperature thresholds<sup>2</sup>. TRPV1, the founding member of the TRPV channels, is a sensor of noxious heat, capsaicin and protons (low pH), and it has been shown to have a key role in nociception in dorsal root ganglions<sup>3–6</sup>. TRPV2 is closely related to TRPV1, sharing high sequence identity (>50%), but TRPV2 exhibits a higher temperature threshold and sensitivity (Q<sub>10</sub>) for activation than does TRPV1 (ref. 7). Furthermore, TRPV2 activity can be modulated by ligands (2-aminoethoxydiphenyl borate (2-APB) and probenecid) or lipids (phosphatidylinositol 4,5-bisphosphate (PIP<sub>2</sub>) and phosphatidylinositol-3-phosphate (PI3P))<sup>8–10</sup>. In addition, an increasing number of studies have suggested that TRPV2 is involved in osmosensation and mechanosensation<sup>11,12</sup>. In contrast to TRPV1, TRPV2 is expressed in both neuronal and non-neuronal tissues, and it has been implicated in diverse physiological and pathophysiological processes, including cardiac-structure maintenance, innate immunity and cancer<sup>8,13–15</sup>.

Recently, structures of TRPV1 have been determined at near-atomic resolution by cryo-EM<sup>16,17</sup>. The architecture of the transmembrane region of TRPV1 is analogous to that of voltage-gated cation channels (VGCCs) and comprises a homotetramer with the ion-permeation pathway located at the four-fold symmetry axis. The transmembrane segment 5 (S5), the pore helix and S6 together form a pore in the assembled tetramer, and a short loop between the pore helix and S6 forms the selectivity filter. Four voltage sensor-like domains (VSLDs), composed of a bundle of four transmembrane helices (S1–S4), surround the central pore. Unlike VGCC, the cytosolic region

is largely composed of an N-terminal ankyrin repeat domain (ARD) and a collection of short structural subdomains that connect the transmembrane and cytosolic regions, which include a linker domain (or membrane-proximal domain), a pre-S1 helix, a TRP domain and a C-terminal domain (CTD). Comparison of the apo (closed), capsaicin-bound (partially open) and DkTx and resiniferatoxin-bound (fully open) TRPV1 structures has shown that TRPV1 contains two gates: the upper gate, formed by the selectivity filter, and the lower gate, formed by the bundle-crossing region at S6. Cryo-EM studies of TRPV1 have demonstrated how toxin binding facilitates the conformational transitions that cause these gates to open, thereby providing a fundamental framework for understanding the structural basis of TRPV1 activation<sup>16,17</sup>. Thus far, structural information on TRPV2 has been limited to crystallographic studies of the ARD and a low-resolution cryo-EM study of the channel<sup>18–20</sup>. This previous cryo-EM study has proposed an arrangement of the ARD assembly that differs significantly from that of TRPV1 (ref. 20).

To understand the structural basis underlying the mechanism of TRPV2 permeation and gating, we set out to determine the TRPV2 structure at a higher resolution. Here, we report the cryo-EM structure of rabbit TRPV2 at ~4-Å resolution, which contains regions that are resolved to 3.3 Å. Our structure adopts a nonconductive state but is structurally distinct from the closed TRPV1 structure. On the basis of comparison with TRPV1 structures, we speculate that the observed structure of TRPV2 represents a desensitized state. This structural study contributes to the expanding conformational landscape of TRPV channels and provides insights into the molecular basis of TRPV-channel gating.

## RESULTS

### Overall architecture and protomer structure of TRPV2

To facilitate structural studies, we generated a truncated version of rabbit TRPV2, which was similar to a previously reported minimal

<sup>1</sup>Department of Biochemistry, Duke University Medical Center, Durham, North Carolina, USA. <sup>2</sup>Department of Integrative Structural and Computational Biology, The Scripps Research Institute, La Jolla, California, USA. <sup>3</sup>These authors contributed equally to this work. Correspondence should be addressed to S.-Y.L. (sylee@biochem.duke.edu) or G.C.L. (glander@scripps.edu).

Received 10 November 2015; accepted 10 December 2015; published online 18 January 2016; doi:10.1038/nsmb.3159

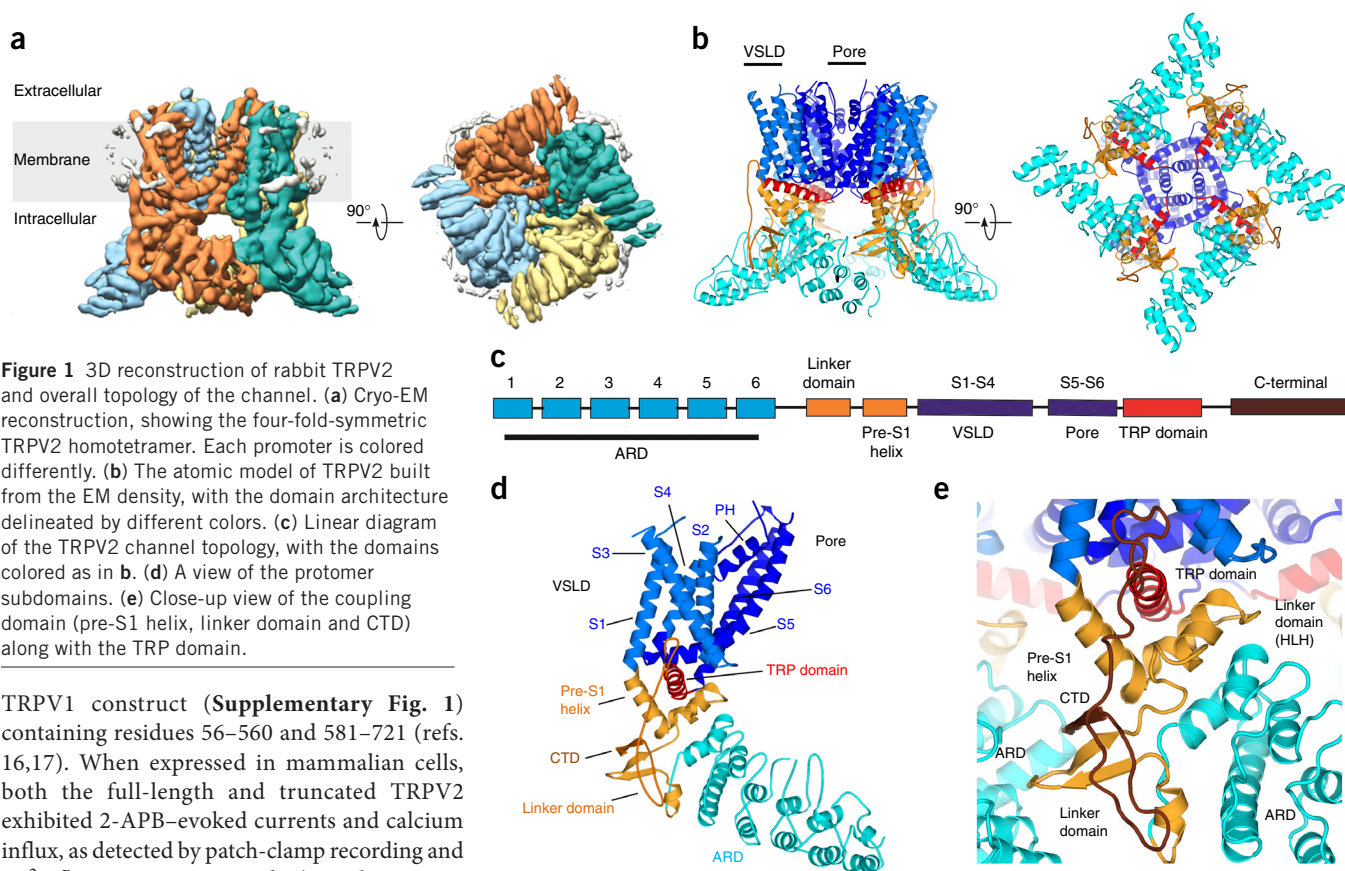


**Figure 1** 3D reconstruction of rabbit TRPV2 and overall topology of the channel. **(a)** Cryo-EM reconstruction, showing the four-fold-symmetric TRPV2 homotetramer. Each protomer is colored differently. **(b)** The atomic model of TRPV2 built from the EM density, with the domain architecture delineated by different colors. **(c)** Linear diagram of the TRPV2 channel topology, with the domains colored as in **b**. **(d)** A view of the protomer subdomains. **(e)** Close-up view of the coupling domain (pre-S1 helix, linker domain and CTD) along with the TRP domain.

TRPV1 construct (**Supplementary Fig. 1**) containing residues 56–560 and 581–721 (refs. 16,17). When expressed in mammalian cells, both the full-length and truncated TRPV2 exhibited 2-APB-evoked currents and calcium influx, as detected by patch-clamp recording and  $\text{Ca}^{2+}$ -flux assay, respectively (**Supplementary Fig. 2**). We determined the structure of truncated TRPV2 to an overall resolution of  $\sim 4.2$  Å for the entire molecule and resolved the transmembrane region to better than 3.8 Å (**Supplementary Figs. 3–5**). The final refined atomic model accounts for  $\sim 90\%$  of the molecule subjected to EM analysis and possesses good overall geometry, with a MolProbity score of 2.3 (**Supplementary Table 1**).

The overall architecture of TRPV2 is identical to that of the TRPV1, as anticipated (**Fig. 1**). Nevertheless, the TRPV2 structure provides an architectural rationale for prior observations that the linker domain (also known as the membrane-proximal domain, Pro320–Leu373) is important for thermosensation<sup>21</sup>. The linker domain is positioned at the nexus of the ARD and the transmembrane helices and establishes a network of contacts between these domains and with the neighboring protomer (**Fig. 1e**). The helix-loop-helix (HLH) of the linker domain, together with the pre-S1 helix, forms a V-shaped cradle that accommodates a helix known as the TRP domain at the membrane-cytosol interface. The HLH, as well as another small helix within the linker domain, additionally contacts the ARD, thus resulting in a tertiary organization that potentially enables the HLH to translate motions within the ARD to the TRP domain. In addition to these contacts, the antiparallel  $\beta$ -sheet of the linker domain interacts with the neighboring ARD (through finger 3 and ankyrin repeats 3 and 4), thus possibly enabling cooperativity between subunits to influence channel gating (**Supplementary Fig. 6a,b**).

Many TRP channels possess a conserved sequence known as the ‘TRP box’, which is located at the C-terminal end of S6, a region important for channel gating and desensitization<sup>22–24</sup>. The TRP domain constitutes a large portion of the TRP box and is sandwiched between the VSLD and the cradle formed by the linker domain and the pre-S1 helix, in a position that allows communication to be established between the transmembrane and the

intracellular regions (**Fig. 1e**). After the TRP domain, the CTD forms an extended loop that is coiled back and contributes a  $\beta$ -strand to the antiparallel  $\beta$ -sheet of the linker domain. This extended loop interacts with the short N-terminal helix of the linker domain as well as the sixth repeat of ARD, thus suggesting that the CTD reinforces the roles of the linker domain in subunit assembly and in linking cytosolic and transmembrane regions (**Fig. 1e** and **Supplementary Fig. 6b**). Chimeric studies have shown that the extended loop and the  $\beta$ -strand region of the CTD are critical for converting the directionality of heat sensitivity in TRPV1 and TRPM8 (refs. 25,26). The CTD was not resolved in the TRPV1 structures, but the high sequence homology between these proteins suggests that this interaction of the CTD with the linker domain is likely to be conserved between TRPV1 and TRPV2. For simplicity, the linker domain, the pre-S1 helix and the CTD will hereafter be referred to as the ‘coupling domain’. The coupling domain, together with the TRP-domain helix, links cytosolic ARD to the transmembrane channel region.

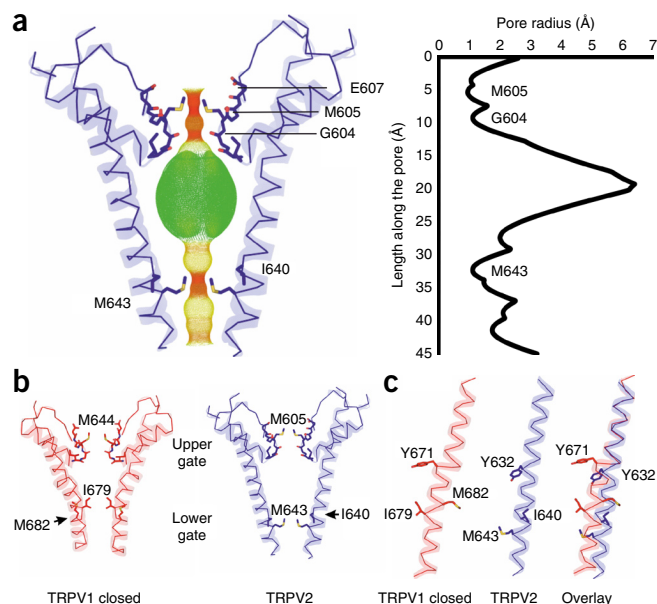
### TRPV2 and TRPV1 have different gates at S6

To investigate the conformational state of the pore, we calculated the pore radius along the permeation pathway with the program HOLE<sup>27</sup>. There are two constriction sites along the central ion-permeation pathway within the pore domain: one at the selectivity filter and the other near the bundle-crossing region of S6 (**Fig. 2a**). The conserved sequence 604-GMGE-607, located between the pore helix and S6, forms the selectivity filter. In our TRPV2 structure, the backbone carbonyl atoms of Gly604 and side chains of Met605 form the narrowest points of the channel, similarly to the structure observed in TRPV1. The distances between the carbonyl oxygens of Gly604 and between the sulfur atoms of Met605 from two diagonally opposing subunits are 5.2 Å and 5.4 Å, respectively, both of which are too narrow

**Figure 2** Pore structure of TRPV2. (a) Profile of the TRPV2 pore generated with HOLE software<sup>27</sup> indicates two main constrictions: one at the selectivity filter formed by the side chains of Met605 and the backbone carbonyls of Gly604, and the second one close to the helix-bundle crossing, formed by the side chains of Met643. (b) Comparison of the pores of the closed TRPV1 and the TRPV2 channels, showing that the lower gate of TRPV1 is formed by Ile679, whereas the lower gate in TRPV2 is one turn lower, at Met643. (c) Comparison of the TRPV1 and TRPV2 S6 helices shows that the S6 helix in TRPV1 contains a  $\pi$ -helical segment, whereas the S6 in TRPV2 is  $\alpha$ -helical.

to allow hydrated cations to permeate<sup>28</sup>. Furthermore, the planar tetra-coordination conferred by the carbonyl atoms of Gly604 cannot bind dehydrated cations ( $\text{Na}^+$ ,  $\text{Ca}^{2+}$  and  $\text{K}^+$ ) optimally, because these cations require higher coordination numbers (6 for  $\text{Na}^+$ , 7 for  $\text{Ca}^{2+}$  and 8 for  $\text{K}^+$ )<sup>29</sup>. The hydrophobic ring formed by Met605, located immediately above the Gly604, probably limits access to water, thereby preventing additional water-mediated coordination of a dehydrated cation, thus indicating that our TRPV2 structure represents a nonconductive state at the selectivity filter.

We observed another constriction site where the Met643 from each subunit forms a hydrophobic seal near the S6 helical bundle-crossing region (Fig. 2a). By contrast, in the closed TRPV1 structure, Ile673 (Ile640 in TRPV2) forms the lower gate, which is located closer to the selectivity filter and further from the bundle-crossing region (Fig. 2b). Interestingly, in the TRPV2 structure, Ile640 does not face the central permeation pathway and thus cannot form the lower gate. To understand the origin of this difference in the lower gate, we overlaid S6 of TRPV1 and TRPV2, revealing that, whereas all existing atomic structures of TRPV1 show that S6 adopts a  $\pi$ -helix in the middle of S6, TRPV2 S6 instead adopts a canonical  $\alpha$  helix conformation (Fig. 2c and Supplementary Fig. 7). The  $\pi$ -helix is a rare secondary-structural element in which the backbone carbonyl of residue  $i$  forms hydrogen bonds to the backbone amide of residue  $i + 5$ , thus resulting in a wider helical turn and a register shift<sup>30</sup>. The presence of a  $\pi$ -helix in TRPV1 causes the C-terminal part of S6 to bend away from the permeation pathway and introduces a helical-register shift of one residue. This difference in secondary structure accounts for the observed disparity in the lower gates of TRPV1 and TRPV2, thus



resulting in positioning of the TRPV2 lower gate closer to the cytosol by one helical turn (Fig. 2c). The S6 is the most conserved region within the TRPV family (Supplementary Fig. 1), and we were not able to identify any differences in the local interaction networks near Tyr671 in TRPV1 or Tyr632 in TRPV2, residues that demarcate the point at which S6 deviates to a  $\pi$ -helix in TRPV1 versus an  $\alpha$ -helix in TRPV2. Together, these data led us to speculate that the high-energy  $\pi$ -helical S6 and the low-energy  $\alpha$ -helical S6 may represent different functional states of the channels.

### The selectivity filter and surrounding interactions

The selectivity filter of our TRPV2 structure adopts a conformation that is nearly identical to that observed in the apo (closed) TRPV1 structure (PDB 3J5P)<sup>17</sup>, whose selectivity gate is shut by the Gly604 backbone carbonyl groups and the side chain atoms of Met605 (Fig. 3a). In the structure of the fully opened TRPV1 (PDB 3J5Q)<sup>16</sup>, the distance between these two residues increases, thus allowing passage of calcium ions, and an aspartate residue (corresponding to Glu607 in TRPV2) moves closer to the central permeation pathway, thereby switching the channel to the conductive state (Fig. 3). This conversion of a closed to an open filter gate is mediated by the rearrangement of the interactions between the turret (the loop between S5 and the pore helix) and the pore loop (the loop between the filter and S6), and multiple studies have supported the importance of these interactions in either heat-mediated or chemically mediated activation of the selectivity-filter gate<sup>31–34</sup>. Indeed, in TRPV1, the interaction network that maintains the turret and the pore loop in tight contact in the closed state is disrupted in the open state, which allows the pore helix and the selectivity filter to move away from the permeation pathway (Fig. 3). Interestingly, this network between the pore loop and the turret in the TRPV2 structure is disrupted, although

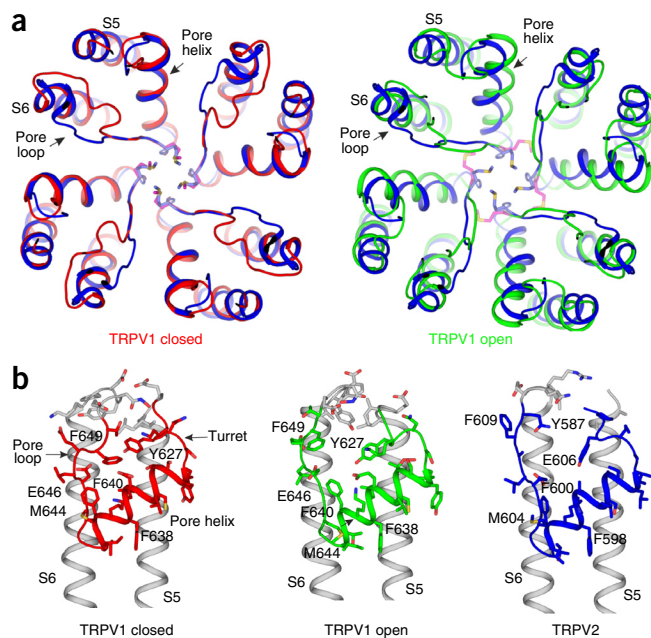


**Figure 3** Comparison of the pore-helix and pore-loop regions of TRPV1 and TRPV2. (a) Top view of the channel pore. The pore helix of TRPV2 (blue) and the closed TRPV1 channel (red) are in the same conformation, whereas the pore loop of TRPV2 adopts a conformation more similar to that of the open TRPV1 channel (green). Methionine residues of the selectivity filters of the closed and open TRPV1 (red and pink, respectively) and TRPV2 (blue) are shown in stick representation. (b) View of the coupling between the pore loop and turret in the closed TRPV1 structure (red), open TRPV1 structure (green) and TRPV2 structure (blue).

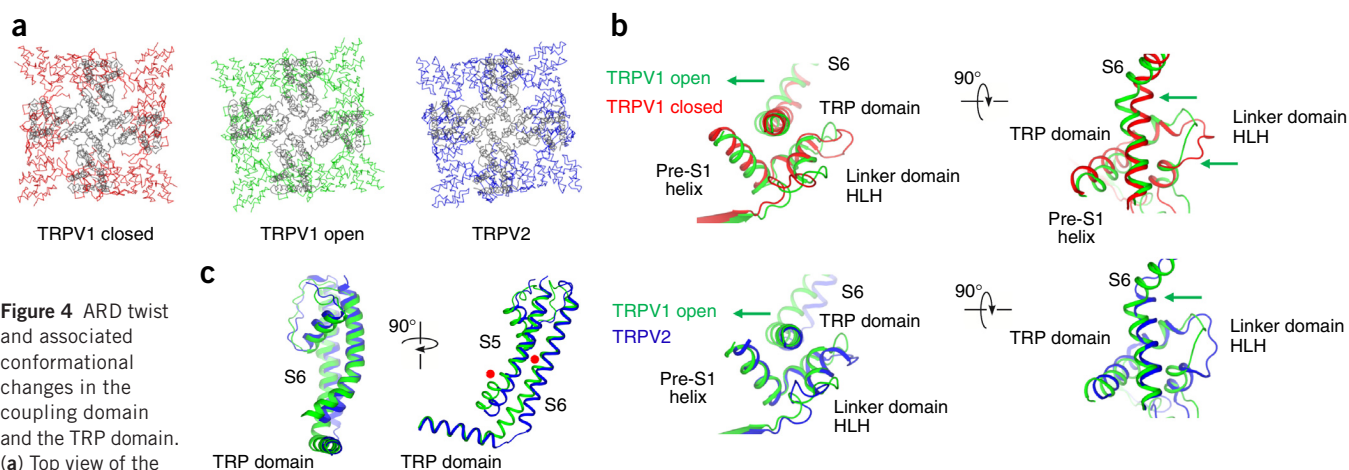


**Figure 4** ARD twist and associated conformational changes in the coupling domain and the TRP domain. (a) Top view of the TRPV1 and TRPV2 channels.

Overlay of the pore domains (gray) of the closed TRPV1, open TRPV1 and TRPV2 channels, indicating that the ARD of the open TRPV1 and TRPV2 have undergone a counterclockwise rotation relative to the closed TRPV1. (b) Close-up comparison of the pre-S1 helix, the linker and TRP domain of the open TRPV1 (green) with the closed TRPV1 (red) and with the TRPV2 channel (blue). TRPV1 undergoes a conformational change in the linker domain and a displacement of the part of the TRP domain closest to S6. The helices of the HLH region in TRPV2 assume a similar conformation to that observed in the open TRPV1, but the connecting loop is in a different position. The position of the TRP domain in TRPV2 is different from that in both closed and open TRPV1. Green arrows indicate the motions of the open TRPV1 S6 and the linker domain (HLH) compared to the closed TRPV1 and TRPV2, respectively. (c) Comparison of the coupling between S6 and the TRP domain in the open (green) TRPV1 and the TRPV2 (blue) channels. The positions of  $\pi$ -helices in both S6 and the junction between S5 and the S4-S5 linker in TRPV1 are indicated (red dots).

the pore helix and the selectivity filter assume a conformation that is nearly identical to that of the closed TRPV1.

Although these observations may suggest that the pore loop and the turret in TRPV2 are decoupled from the selectivity filter (Fig. 3b and Supplementary Fig. 8a,b), it is important to note that the distal part of the pore loop and the turret are not well conserved between TRPV channels. It is therefore unclear whether the different conformation around the selectivity filter of TRPV2 is due to a difference in sequence or whether it reflects a previously unobserved functional state that is distinct from the closed TRPV1 conformation. Both TRPV1 and TRPV2 constructs have a deletion in the turret region (Supplementary Fig. 1), but these deletions do not appear to have significant functional effects (Supplementary Fig. 2 and ref. 17).

### Comparison with TRPV1 ARD and linker domain

The ARD adopts a conformation that is largely similar to that in the previously reported TRPV2 ARD crystal structure (C $\alpha$  r.m.s. deviation of 1.8 Å with PDB 2ETA<sup>18</sup>, chain A) but structurally diverges in the finger loops 1–3 and ankyrin repeat 1 (Supplementary Fig. 6c).

The previous 13.6-Å-resolution cryo-EM study of TRPV2 (ref. 20) has proposed an arrangement of the ARD assembly that is substantially different from that of TRPV1 and the TRPV2 structure presented herein. In our TRPV2 structure, the ARD assembly is similar to TRPV1 in that the  $\beta$ -sheet from the coupling domain (linker domain and the CTD) interacts with finger 3 and the fourth ankyrin repeat of a neighboring ARD (Fig. 1e and Supplementary Fig. 6). The  $\beta$ -sheet

turn that contacts the neighboring ARD is composed of a GPY motif, which is highly conserved among the members of TRPV family<sup>17</sup>.

Superposition of the pore domains of the closed and the fully open TRPV1 structures revealed that the ARD assembly of the open structure undergoes a counterclockwise twist relative to the transmembrane region when viewed from the extracellular side (Fig. 4a). A close-up view of the two superposed structures suggested that the ARD twist is associated with the conformational change of the linker domain, thus supporting the notion that these domains are tightly linked through a network of interactions (Fig. 4b). This twisting motion of the ARD and the associated movement of the linker domain appear to trigger a swivel of the TRP domain, which in turn exerts a force on S6

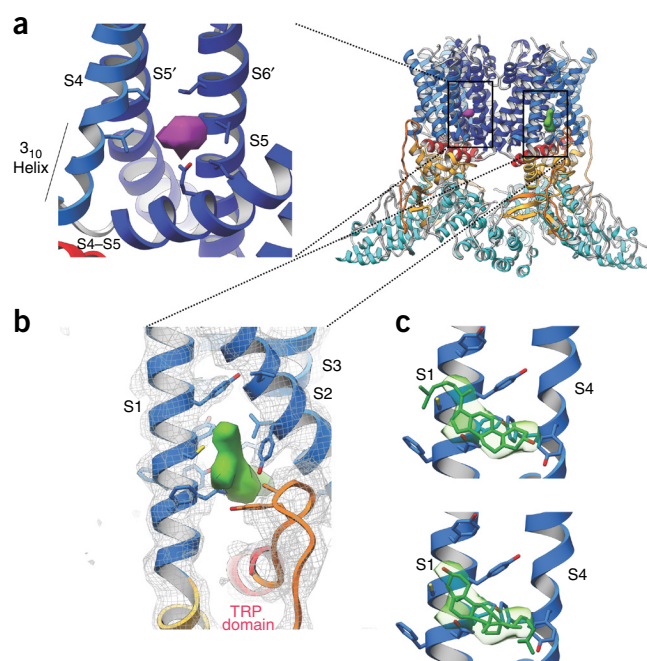


**Figure 5** Putative lipid densities in the TRPV2 map. The cartoon shows the location of the density peaks in the global context. (a) View showing the density (purple) observed in the pocket between subunits formed by S4 and the S4-S5 linker of one subunit and S5 and S6 of the adjacent subunit, as well as the 3<sub>10</sub> helical segment observed in the lower part of S4 (S4b). (b) Density above the coupling domain-TRP domain nexus, between helices S1 and S2. (c) A cholesterol molecule docked into the density with two possible orientations, with a local CC of 0.65 (top) and 0.51 (bottom) between the reciprocal-space reflections filtered at 4 Å and the docked cholesterol molecule. S2 and S3 were removed for clarity.

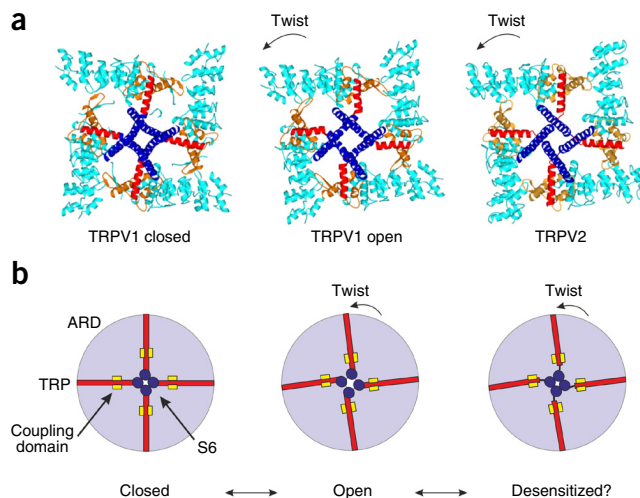
**Figure 6** Coupling between the TRP domain and S6. (a) Top view of the closed TRPV1, open TRPV1 and TRPV2 structures. S1–S5 have been removed for simplicity. Rotation of ARD (cyan) leads to a displacement of the TRP domain (red), which pulls on the S6 (blue) and thereby drives the opening of the lower gate. In TRPV2, the coupling between S6 and the TRP domain is disrupted, and the ARD rotation is therefore not translated to an opening of the channel. (b) Cartoon of the proposed gating mechanism in TRPV channels. The rotation of ARD (light blue circle) is directly coupled to opening of the lower gate through the TRP domain (red). This coupling is guided by the pre-S1 helix, the linker domain and CTD, which we collectively refer to as the ‘coupling domain’ (yellow square).

through the helical linker and causes the lower gate to open (Fig. 4b). Inspection of this region revealed that the HLH of the linker domain, which contacts both the TRP domain and ARD, undergoes a conformational change in the transition from the closed to open state, thus implicating the HLH in regulation of the TRP domain (Fig. 4b).

Similarly, a superposition of the transmembrane domains of TRPV2 and closed TRPV1 showed a twisting motion of the TRPV2 ARD that is analogous to the movement observed from the closed state to the open state of TRPV1 (Fig. 4a). However, despite the similar twisting of the ARD, the TRPV2 structure is closed at the lower gate, as described above (Fig. 2a). In order to investigate the mechanism by which similar twists in the ARD assemblies can lead to two different permeant states, we examined the TRP domain, S6 and the coupling between them. Interestingly, in TRPV2 we observed a repositioning of the TRP domain, which appeared to have moved toward the intracellular side at the proximal end of S6 (Supplementary Fig. 8c). Furthermore, in TRPV1, S6 and the TRP domain form a nearly continuous helical structure, whereas in TRPV2, S6 is connected to the TRP domain via a loop, thus indicating that there is a lower degree of coupling between these helices in TRPV2 (Fig. 4c and Supplementary Fig. 8d). A possible explanation for this difference might be in the secondary structure of the S6 helix. Introducing a  $\pi$ -segment into the TRPV2 S6 helix would accommodate the formation of a continuous helical structure between the S6 and the TRP domain, thus resulting in a coupling that is similar to what is observed in the fully open TRPV1 channel (Fig. 4c). This comparison allows us to speculate that the different functional states of the fully open TRPV1 and the TRPV2 may stem from a reorganization of the S6 secondary structure that consequently influences its coupling with the TRP domain.

### Putative lipid-binding sites in the TRPV2 structure

During structure refinement, we identified two densities that could not be assigned to polypeptide. We observed a prominent density near the C-terminal portion of S4 (S4b, Asn509–Arg515), the S4–S5 linker and S6 of an adjacent subunit (Fig. 5a), at a position similar to that of capsaicin and resiniferatoxin in the TRPV1 structures<sup>16</sup>. TRPV1 is the only member of the TRPV family that is activated by capsaicin, thus suggesting that this density observed in our TRPV2 structure may correspond to a weakly ordered lipid molecule. Studies have shown that Thr551 in S4 and Glu571 in the S4–S5 linker are critical residues for capsaicin binding in TRPV1 (refs. 35,36), but the corresponding residues in TRPV2 are leucine and glutamine, respectively, thus potentially explaining why TRPV2 is not responsive to capsaicin (Supplementary Fig. 1). A weak density at this location is present in the closed TRPV1 structure in the absence of capsaicin (EMD-5778) (ref. 17), thus suggesting that under physiological conditions, this site might be occupied by a lipid molecule in both TRPV1 and TRPV2, and that replacement of the lipid with capsaicin or resiniferatoxin might help stabilize the open state of TRPV1.



Notably, the lipid-, capsaicin- or toxin-binding site includes S4b, which contains two full turns of a  $3_{10}$  helix in TRPV2 (Fig. 5a and Supplementary Fig. 7c). This architecture is reminiscent of S4b in VGCCs, which has an unusually long stretch of  $3_{10}$  helix 7–11 amino acids long. In VGCCs, the presence of an energetically less stable  $3_{10}$  helix confers mobility to S4 (refs. 37,38). The TRPV1 structures also possess a  $3_{10}$  helix at S4b; however, unlike VGCCs, the VSLD in TRPV1 is believed to be static<sup>16,17</sup>. This suggests that the  $3_{10}$  helical feature of S4b may confer mobility to both S4b and the S4–S5 linker in these channels. In agreement with this hypothesis, the junction between the S4–S5 linker and S5 in the fully open TRPV1 contains a  $\pi$ -helical configuration, whereas this junction in TRPV2 is  $\alpha$ -helical (Fig. 4c and Supplementary Fig. 7d). This structural difference suggests a dynamic interplay between S4b and the S4–S5 linker, as well as interactions with both S6 and the TRP domain.

Another larger density is located in the crevice formed by the S1–S4 helical bundle, directly above the TRP domain and the coupling-domain nexus, a region with a critical role in channel gating (Fig. 5b). We hypothesize that this density may correspond to a lipid molecule that was copurified with the channel protein, because lipids were included in the preparation of TRPV2 (Online Methods). Considering the shape of this electron density peak, we speculate that it might correspond to a cholesterol molecule (Fig. 5c). We found that a similar electron density peak at the analogous position is present in the closed TRPV1 structure<sup>17</sup>. Notably, without the putative lipid molecule in this crevice, there would be a large gap between the TRP domain and the rest of the VSLD (Fig. 5b). Because of the critical role of the TRP domain in channel function, it is possible that a molecule that would bind here might have a role in the modulation of channel function.

After the TRP-domain helix in TRPV1, there is a loop with a sharp turn toward the intracellular site; we were unable to model this loop, owing to a lack of ordered density in this region. Multiple studies have shown that this loop region near the TRP-domain helix is the binding site for PIP<sub>2</sub>, which includes Arg721 in TRPV1 (Arg682 in TRPV2), a key residue for PIP<sub>2</sub> binding<sup>6</sup>. In our TRPV2 structure, this loop takes a wide turn after the TRP-domain helix and terminates by adding a  $\beta$ -strand to the  $\beta$ -sheet within the linker domain (Fig. 1e). Although the lower resolution of this region prevented accurate modeling of side chains, several arginine and lysine residues from pre-S1, S1, S2 and the CTD loop may create a favorable environment for binding negatively charged lipids, such as PIP<sub>2</sub> and PI3P (Supplementary Fig. 6d).

## DISCUSSION

Comparison to the TRPV1 structures guided our interpretation of the functional state of the TRPV2 structure presented here. In TRPV1, the relayed (or concerted) motion of the ARD assembly, coupling domain, TRP domain and S6 appears to be important for opening of the lower gate at S6 (Fig. 6a,b), a result consistent with findings from many functional studies that underscore the importance of ARD, the coupling domain and the TRP domain in heat- and ligand-dependent gating<sup>21,22,26,39,40</sup>. In our structure of TRPV2, the selectivity-filter gate in TRPV2 is closed, but the lack of tight interactions between the pore loop and the turret is similar to the characteristics of the fully open TRPV1 structure. In addition, although the ARD assembly in TRPV2 is rotated relative to the transmembrane region—similarly to the ARD rotation observed in the fully open TRPV1—the coupling interactions between the TRP domain and S6 in TRPV2 appear to be loose. This lack of coupling may be due to the absence of a  $\pi$ -helix in S6, thus resulting in a nonconductive state that is distinct from the closed TRPV1 structure.

From our observations, we propose that our TRPV2 structure represents a desensitized state. It is possible that S6 in TRPV2 adopts a  $\pi$ -helical configuration in a conductive state. All the VGCCs contain highly conserved glycine or proline residues in S6, which facilitate the hinge bending in S6 that is essential to opening the S6 bundle-crossing gate<sup>37</sup>. Because TRPV channels lack a corresponding glycine or proline in S6, we hypothesize that a  $\pi$ -helical configuration in the middle of S6 serves a similar purpose in TRPV channels and is essential for gate opening. It is plausible that during desensitization S6 may switch from a high-energy configuration ( $\pi$ -helix) to a low-energy configuration ( $\alpha$ -helix), thereby leading to straightening and rotation of S6 and resulting in a shift of the lower gate to a different position. This shift would prevent the gate opening, cause unwinding of the helical linker between the S6 and the TRP domain and consequently lead to decoupling of the ARD and gate (Fig. 6a,b and Supplementary Movie 1). Our hypothetical mechanism of desensitization is consistent with results from studies showing that the TRP domain is critical for both heat- and ligand-dependent desensitization in TRPV1 (ref. 23). Notably, previous evidence supports TRPV2 desensitization in the absence of PIP<sub>2</sub> (ref. 40), and because we did not supplement with PIP<sub>2</sub> during purification, it is possible that a sizable fraction of the protein may have been purified in a desensitized state.

However, we cannot rule out an alternate model in which our TRPV2 structure represents a different closed, nondesensitized state than that observed for TRPV1. In that case, the transition from the closed state to the open state in TRPV2 would involve a conversion from a low-energy  $\alpha$ -helical S6 to a high-energy  $\pi$ -helical S6. Perhaps the energy gained by an increase in either temperature or ligand binding would help to shift this conversion. This scenario is consistent with a higher temperature threshold and sensitivity ( $Q_{10}$ ) for activation of TRPV2 compared to TRPV1 (ref. 21).

## METHODS

Methods and any associated references are available in the [online version of the paper](#).

**Accession codes.** Coordinates have been deposited in the Protein Data Bank under accession code PDB 5AN8, and the electron density maps have been deposited in the Electron Microscopy Data Bank under accession code EMD-6455.

*Note: Any Supplementary Information and Source Data files are available in the [online version of the paper](#).*

## ACKNOWLEDGMENTS

Cryo-EM data were collected at the electron microscopy facility at The Scripps Research Institute. We are indebted to J. Grandl and J. Sosa, who provided access to their calcium-imaging apparatus and guidance in calcium-imaging experiments. We thank J.-C. Ducom at The Scripps High Performance Computing facility for aiding with computational needs, S. Thomas and Z. Ouyang for initial TRPV2 biochemistry and E. Mashalidis for advice on the manuscript. This work was supported by start-up funds from the Duke University Medical Center (S.-Y.L.) and the US National Institutes of Health (R01GM100894 and DP2OD008380 to S.-Y.L., and DP2EB020402 to G.C.L.). G.C.L. is supported as a Searle Scholar and a Pew Scholar.

## AUTHOR CONTRIBUTIONS

L.Z. conducted all biochemical preparation of TRPV2 and calcium-imaging experiments under the guidance of S.-Y.L. M.A.H. conducted all electron microscopy experiments and the single-particle 3D reconstruction under the guidance of G.C.L., B.C.C. and L.Z. S.-Y.L. carried out model building and refinement. Z.L. performed electrophysiology experiments. L.Z., M.A.H., G.C.L. and S.-Y.L. wrote the manuscript.

## COMPETING FINANCIAL INTERESTS

The authors declare no competing financial interests.

Reprints and permissions information is available online at <http://www.nature.com/reprints/index.html>.

- Ramsey, I.S., Delling, M. & Clapham, D.E. An introduction to TRP channels. *Annu. Rev. Physiol.* **68**, 619–647 (2006).
- Bandell, M., Macpherson, L.J. & Patapoutian, A. From chills to chills: mechanisms for thermosensation and chemesthesis via thermoTRPs. *Curr. Opin. Neurobiol.* **17**, 490–497 (2007).
- Caterina, M.J. *et al.* The capsaicin receptor: a heat-activated ion channel in the pain pathway. *Nature* **389**, 816–824 (1997).
- Julius, D. TRP channels and pain. *Annu. Rev. Cell Dev. Biol.* **29**, 355–384 (2013).
- Cao, E., Cordero-Morales, J.F., Liu, B., Qin, F. & Julius, D. TRPV1 channels are intrinsically heat sensitive and negatively regulated by phosphoinositide lipids. *Neuron* **77**, 667–679 (2013).
- Ufret-Vincenty, C.A. *et al.* Mechanism for phosphoinositide selectivity and activation of TRPV1 ion channels. *J. Gen. Physiol.* **145**, 431–442 (2015).
- Caterina, M.J., Rosen, T.A., Tominaga, M., Brake, A.J. & Julius, D. A capsaicin-receptor homologue with a high threshold for noxious heat. *Nature* **398**, 436–441 (1999).
- Perálvarez-Marín, A., Doñate-Macian, P. & Gaudet, R. What do we know about the transient receptor potential vanilloid 2 (TRPV2) ion channel? *FEBS J.* **280**, 5471–5487 (2013).
- Qin, N. *et al.* TRPV2 is activated by cannabidiol and mediates CGRP release in cultured rat dorsal root ganglion neurons. *J. Neurosci.* **28**, 6231–6238 (2008).
- Penna, A. *et al.* PI3-kinase promotes TRPV2 activity independently of channel translocation to the plasma membrane. *Cell Calcium* **39**, 495–507 (2006).
- Shibasaki, K., Murayama, N., Ono, K., Ishizaki, Y. & Tominaga, M. TRPV2 enhances axon outgrowth through its activation by membrane stretch in developing sensory and motor neurons. *J. Neurosci.* **30**, 4601–4612 (2010).
- Zanou, N. *et al.* Osmosensation in TRPV2 dominant negative expressing skeletal muscle fibres. *J. Physiol.* **593**, 3849–3863 (2015).
- Katanosaka, Y. *et al.* TRPV2 is critical for the maintenance of cardiac structure and function in mice. *Nat. Commun.* **5**, 3932 (2014).
- Link, T.M. *et al.* TRPV2 has a pivotal role in macrophage particle binding and phagocytosis. *Nat. Immunol.* **11**, 232–239 (2010).
- Monet, M. *et al.* Role of cationic channel TRPV2 in promoting prostate cancer migration and progression to androgen resistance. *Cancer Res.* **70**, 1225–1235 (2010).
- Cao, E., Liao, M., Cheng, Y. & Julius, D. TRPV1 structures in distinct conformations reveal activation mechanisms. *Nature* **504**, 113–118 (2013).
- Liao, M., Cao, E., Julius, D. & Cheng, Y. Structure of the TRPV1 ion channel determined by electron cryo-microscopy. *Nature* **504**, 107–112 (2013).
- Jin, X., Touhey, J. & Gaudet, R. Structure of the N-terminal ankyrin repeat domain of the TRPV2 ion channel. *J. Biol. Chem.* **281**, 25006–25010 (2006).
- McCleverty, C.J., Koesema, E., Patapoutian, A., Lesley, S.A. & Kreuzsch, A. Crystal structure of the human TRPV2 channel ankyrin repeat domain. *Protein Sci.* **15**, 2201–2206 (2006).
- Huynh, K.W. *et al.* Structural insight into the assembly of TRPV channels. *Structure* **22**, 260–268 (2014).
- Yao, J., Liu, B. & Qin, F. Modular thermal sensors in temperature-gated transient receptor potential (TRP) channels. *Proc. Natl. Acad. Sci. USA* **108**, 11109–11114 (2011).
- Gregorio-Tuerel, L. *et al.* The integrity of the TRP domain is pivotal for correct TRPV1 channel gating. *Biophys. J.* **109**, 529–541 (2015).
- Joseph, J., Wang, S., Lee, J., Ro, J.Y. & Chung, M.K. Carboxyl-terminal domain of transient receptor potential vanilloid 1 contains distinct segments differentially involved in capsaicin- and heat-induced desensitization. *J. Biol. Chem.* **288**, 35690–35702 (2013).
- Ufret-Vincenty, C.A., Klein, R.M., Hua, L., Angueyra, J. & Gordon, S.E. Localization of the PIP2 sensor of TRPV1 ion channels. *J. Biol. Chem.* **286**, 9688–9698 (2011).

25. Brauchi, S., Orta, G., Salazar, M., Rosenmann, E. & Latorre, R. A hot-sensing cold receptor: C-terminal domain determines thermosensation in transient receptor potential channels. *J. Neurosci.* **26**, 4835–4840 (2006).
26. Brauchi, S. *et al.* Dissection of the components for PIP<sub>2</sub> activation and thermosensation in TRP channels. *Proc. Natl. Acad. Sci. USA* **104**, 10246–10251 (2007).
27. Smart, O.S., Neduvellil, J.G., Wang, X., Wallace, B.A. & Sansom, M.S. HOLE: a program for the analysis of the pore dimensions of ion channel structural models. *J. Mol. Graph.* **14**, 354–360, 376 (1996).
28. Tang, L. *et al.* Structural basis for Ca<sup>2+</sup> selectivity of a voltage-gated calcium channel. *Nature* **505**, 56–61 (2014).
29. Gouaux, E. & Mackinnon, R. Principles of selective ion transport in channels and pumps. *Science* **310**, 1461–1465 (2005).
30. Cooley, R.B., Arp, D.J. & Karplus, P.A. Evolutionary origin of a secondary structure:  $\pi$ -helices as cryptic but widespread insertional variations of  $\alpha$ -helices that enhance protein functionality. *J. Mol. Biol.* **404**, 232–246 (2010).
31. Grandl, J. *et al.* Temperature-induced opening of TRPV1 ion channel is stabilized by the pore domain. *Nat. Neurosci.* **13**, 708–714 (2010).
32. Jordt, S.E., Tominaga, M. & Julius, D. Acid potentiation of the capsaicin receptor determined by a key extracellular site. *Proc. Natl. Acad. Sci. USA* **97**, 8134–8139 (2000).
33. Cui, Y. *et al.* Selective disruption of high sensitivity heat activation but not capsaicin activation of TRPV1 channels by pore turret mutations. *J. Gen. Physiol.* **139**, 273–283 (2012).
34. Ryu, S., Liu, B., Yao, J., Fu, Q. & Qin, F. Uncoupling proton activation of vanilloid receptor TRPV1. *J. Neurosci.* **27**, 12797–12807 (2007).
35. Yang, F. *et al.* Structural mechanism underlying capsaicin binding and activation of the TRPV1 ion channel. *Nat. Chem. Biol.* **11**, 518–524 (2015).
36. Jordt, S.E. & Julius, D. Molecular basis for species-specific sensitivity to “hot” chili peppers. *Cell* **108**, 421–430 (2002).
37. Long, S.B., Tao, X., Campbell, E.B. & MacKinnon, R. Atomic structure of a voltage-dependent K<sup>+</sup> channel in a lipid membrane-like environment. *Nature* **450**, 376–382 (2007).
38. Vieira-Pires, R.S. & Morais-Cabral, J.H. 3<sub>10</sub> helices in channels and other membrane proteins. *J. Gen. Physiol.* **136**, 585–592 (2010).
39. Lishko, P.V., Procko, E., Jin, X., Phelps, C.B. & Gaudet, R. The ankyrin repeats of TRPV1 bind multiple ligands and modulate channel sensitivity. *Neuron* **54**, 905–918 (2007).
40. Mercado, J., Gordon-Shaag, A., Zagotta, W.N. & Gordon, S.E. Ca<sup>2+</sup>-dependent desensitization of TRPV2 channels is mediated by hydrolysis of phosphatidylinositol 4,5-bisphosphate. *J. Neurosci.* **30**, 13338–13347 (2010).

## ONLINE METHODS

**Protein expression and purification.** Rabbit TRPV2 showed optimal stability for structure determination, on the basis of a screen of 48 TRPV2 orthologs. The codon-optimized gene for the full-length rabbit TRPV2 was synthesized, and the truncated rabbit TRPV2 construct, containing residues 56–560 and 581–721, was cloned into a pFastBac vector in frame with a FLAG affinity tag, and baculovirus was produced according to the manufacturer's protocol (Invitrogen, Bac-to-Bac). For protein expression, Sf9 insect cells were infected with baculovirus at a density of  $1.3 \text{ M cells ml}^{-1}$  and grown at  $27^\circ\text{C}$  for 72 h in an orbital shaker. After 72 h, cell pellets were collected, resuspended in buffer A (50 mM Tris, pH 8, 150 mM NaCl,  $1 \mu\text{g ml}^{-1}$  leupeptin,  $1.5 \mu\text{g ml}^{-1}$  pepstatin,  $0.84 \mu\text{g ml}^{-1}$  aprotinin, 0.3 mM PMSE, 14.3 mM  $\beta$ -mercaptoethanol, and DNase I) and lysed by sonication ( $3 \times 30$  pulses). For extraction, 40 mM DDM and 4 mM cholesteryl hemisuccinate (CHS) Tris salt (Anatrace) were added to the lysate at  $4^\circ\text{C}$  for 1 h. Insoluble material was removed by centrifugation (8,000g, 30 min), and anti-FLAG resin was added to the supernatant for 1 h at  $4^\circ\text{C}$ . After incubation, the resin was washed with ten column volumes of buffer B (50 mM Tris, pH 8, 150 mM NaCl, 1 mM DDM, 0.1 mM CHS, and 10 mM DTT) and eluted with five column volumes of buffer C (50 mM Tris, pH 8, 150 mM NaCl, 1 mM DDM, 0.1 mM CHS,  $0.1 \text{ mg ml}^{-1}$  3:1:1 1-palmitoyl-2-oleoyl-*sn*-glycero-3-phosphocholine (POPC)/1-palmitoyl-2-oleoyl-*sn*-glycero-3-phosphoethanolamine (POPE)/1-palmitoyl-2-oleoyl-*sn*-glycero-3-phospho-(1'-*rac*-glycerol) (POPG), and 10 mM DTT). The FLAG tag was removed overnight by PreScission protease treatment. After size-exclusion chromatography, the protein peak was collected, mixed with Amphipol A8-35 (1:10 w/w ratio) and incubated for 4 h at  $4^\circ\text{C}$  with gentle agitation. Detergent was removed with Bio-Beads SM-2 ( $15 \text{ mg ml}^{-1}$ ) overnight at  $4^\circ\text{C}$ . The reconstituted protein was further purified on a Superose 6 column in PBS, pH 7.6. The primary protein peak was subjected to cryo-EM analysis.

**Sample preparation for EM analysis.** Negative-stained TRPV2 was prepared by application of  $5 \mu\text{l}$  TRPV2 ( $\sim 5 \mu\text{g ml}^{-1}$ ) to a freshly glow-discharged 400-mesh Cu-Rh Maxtaform grid (Electron Microscopy Services) that had been coated with a thin layer of carbon. After incubation for  $\sim 60$  s, excess protein was wicked off with a piece of filter paper, and  $5 \mu\text{l}$  of 1% (w/v) uranyl formate solution was added directly to the grid. After  $\sim 30$  s, excess stain was wicked off with a piece of filter paper, and the grid was immediately inverted and placed on a  $25\text{-}\mu\text{l}$  droplet of 2% (w/v) uranyl formate solution. After 30 s, excess stain was wicked off the grid with filter paper and placed on a fresh  $25\text{-}\mu\text{l}$  droplet of 2% (w/v) uranyl formate solution. This staining process was repeated three times for thorough embedding of the sample, and the grid was subsequently blotted to dryness. Grids were placed on the edge of a fume hood to air-dry after the last blotting step.

For cryo-EM,  $3 \mu\text{l}$  of amphipol-solubilized TRPV2 at a concentration of  $1 \text{ mg ml}^{-1}$  was applied to a freshly glow-discharged 400-mesh C-flat holey carbon grid (Protochips;  $1.2\text{-}\mu\text{m}$ -diameter holes spaced  $1.3 \mu\text{m}$  apart) and blotted with a CP3 (Gatan; 2.5-s blot time,  $\geq 95\%$  relative humidity) before being plunge frozen into liquid ethane cooled by liquid nitrogen.

**EM data acquisition and image processing.** All negative-stained and cryo-EM data were acquired with the Leginon automated data-acquisition program<sup>41</sup>. All image preprocessing and initial 2D classification was performed concurrently with data collection with the Appion image-processing pipeline<sup>42</sup>. The contrast transfer function (CTF) of each micrograph was estimated with CTFFindv3 (ref. 43).

Data acquisition for negative-stained TRPV2 was performed on a Tecnai Spirit (FEI) transmission electron microscope operating at 120 keV. Images were collected at a nominal magnification of 52,000 $\times$  on an F416 CMOS  $4\text{K} \times 4\text{K}$  camera (TVIPS), corresponding to a pixel size of  $2.05 \text{ \AA/pixel}$  at specimen level. All micrographs were collected with an electron dose of  $25 \text{ electrons/\AA}^2$  with a defocus range from  $0.5 \mu\text{m}$  to  $1.2 \mu\text{m}$ . 282 negative-stain EM images were used for automated particle picking with the program Difference of Gaussians (DoG) Picker<sup>44</sup>, thus yielding 22,679 particles. Micrographs were phase-flipped with EMAN<sup>45</sup>, and particles were extracted with a box size of 128 pixels. Pixels with values  $4.5\sigma$  above or below the mean were replaced by noise within  $1\sigma$  of the mean, and the particle images were binned  $2 \times 2$  ( $4.10 \text{ \AA/pixel}$ ). This stack of particles was then subjected to five rounds of reference-free 2D classification with multivariate statistical analysis (MSA) and multireference alignment (MRA) in Appion<sup>46</sup>. Particles belonging to classes that represented nonparticles

or aggregates were eliminated, thus resulting in a stack of 17,033 particles for 3D classification in RELION<sup>47</sup>. A  $60\text{-}\text{\AA}$  low-pass-filtered 3D EM map of TRPV1 (EMD-5778) was used as a starting model for 3D classification, with a  $k$  value of 3 (ref. 17). The class showing the highest level of structural detail was refined with RELION to yield a TRPV2 structure at  $20 \text{ \AA}$  resolution, according to a Fourier shell correlation (FSC) with a 0.143 cutoff.

Cryo-EM images of frozen hydrated TRPV2 were collected at liquid-nitrogen temperature on a Titan Krios transmission electron microscope (FEI) operated at 300 keV and equipped with a K2 Summit camera (Gatan) operating in super-resolution mode (super-resolution pixel size of  $0.65 \text{ \AA/pixel}$ ) (Supplementary Fig. 3). 1,714 movie-mode images were acquired at a nominal magnification of 22,500 $\times$  with a physical pixel size of  $1.31 \text{ \AA/pixel}$  at specimen level and a defocus ranging from  $1.2 \mu\text{m}$  to  $3 \mu\text{m}$ . Each movie comprised 50 frames acquired over 10 s with a dose rate of 9.9 electrons/pixel/s, thus yielding a cumulative dose of  $\sim 57 \text{ electrons/\AA}^2$ . Super-resolution image stacks images were first Fourier-binned  $2 \times 2$ , thus resulting in a pixel size of  $1.31 \text{ \AA}$  for motion correction with the *dosegpu\_driftcorr* program, which used a B factor of 1,000 and a frame offset of 7 (ref. 48). The sum of the motion-corrected subframes from each image stack was used for further processing. Masks were manually drawn around carbon edges and large contaminants to exclude these regions from particle selection. DoGPicker was used to automatically pick particles from the first 43 micrographs, and a stack of 6,306 particles was extracted with a box size of 224 pixels and subjected to reference-free 2D classification with MSA/MRA after binning to a pixel size of  $2.62 \text{ \AA/pixel}$ <sup>46</sup>. The selected representative/unique class averages were designated for template-based particle picking with FindEM<sup>49</sup> against the first 72 images, thus yielding a stack of 9,234 particles, which were classified by MSA/MRA to produce the templates that were used to template-pick the entire data set. The 1,090 micrographs showing a CC  $\geq 80\%$  at a resolution of  $4 \text{ \AA}$  or better were used to extract 524,371 particles with a box size of 256 pixels. This stack of particles was then subjected to reference-free 2D clustering with a topology-representing network<sup>46</sup> to rapidly identify nonparticles, aggregates, or poorly aligned particles. The remaining 427,360 particles, which showed secondary-structural elements when analyzed with 2D reference-free classification in RELION<sup>47</sup>, were used for 3D classification (Supplementary Fig. 4).

All 3D classification and refinement were carried out with RELION version 1.4 beta<sup>47</sup> (Supplementary Fig. 4). The 3D reconstruction from negatively stained TRPV2 was low-pass filtered to  $60 \text{ \AA}$  and used as the starting model for frozen hydrated TRPV2. After 25 iterations of 3D classification into five classes with data binned  $8 \times 8$  ( $5.24 \text{ \AA/pixel}$ ), particles in the classes that produced 3D reconstructions that exhibited the highest levels of structural detail, 183,551 particles in total (43% of the data set), were combined for 3D autorefinement with the data binned  $2 \times 2$  ( $1.31 \text{ \AA/pixel}$ ) with C4 symmetry imposed. Particle movement and radiation damage resulting from exposure to the electron beam was mitigated with the 'particle polishing' procedure implemented in RELION. A three-frame running average was used to determine the frequency-dependent contribution of each of the 50 movie frames to the final reconstruction<sup>50</sup>. The smoothed plot of the per-frame B-factor values used to calculate the frequency-dependent weighting is shown in Supplementary Figure 5, and the resulting stack of polished particles was used for further 3D autorefinement. A soft mask that excluded the amphipol cloud was used to estimate the resolution from the two independently refined half data sets, reporting  $4.35 \text{ \AA}$  at an FSC of 0.143 (Supplementary Fig. 5). These particles were then subjected to another round of RELION 3D classification ( $k = 4$ ) without angular or translational searches. Each of the resulting four classes was then further refined with fine angular sampling. The most structurally detailed reconstruction resulted from 43,879 particles (10% of the entire data set), reporting an overall resolution of  $3.85 \text{ \AA}$  (Supplementary Fig. 5). A local resolution calculation with ResMap yielded overestimated values of higher than  $3 \text{ \AA}$  at the core, which is not consistent with the observed structural details. For this reason, a local resolution calculation of this density was performed with the Bsoft package<sup>51</sup>, which showed that regions at the core of the complex were resolved to  $3.3\text{-}\text{\AA}$  resolution (Supplementary Fig. 5). For atomic modeling, a B factor of  $\sim 76 \text{ \AA}^2$  was applied to the unmasked reconstructed density.

**Model building and refinement.** An initial model of the transmembrane regions of TRPV2 was generated in Sculptor (Phenix suite) with the closed TRPV1 structure (PDB 3J5P)<sup>17</sup> and the sequence of rabbit TRPV2 (XP\_002718999.1). The TRPV2 ARD (PDB 2ETA)<sup>18</sup> was docked into the electron density map and

merged with the transmembrane region of the channel to produce a model that covers the entire sequence. The model building was performed manually in Coot<sup>52</sup>. We performed a series of rigid-body fits of structural domains (VSLD, pore, ARD, and the linker domain) and subsequent manual building with Coot. The transmembrane regions were built first because they were well resolved in the electron density map. Many residues with bulky side chains guided the correct helical registers. During the initial manual building, ideal geometry in the backbone and rotamer conformations was imposed as much as possible with Coot. After manual model building, the TRPV2 model was refined with real-space refinement via the command line in PHENIX against the cryo-EM map<sup>53</sup>. Rigid-body and global-minimization strategy were used in real-space refinement with the secondary-structure restraints. After real-space refinement, reciprocal-space refinement was performed with the vector difference refinement mode of REFMAC5 v5.8 (ref. 54). The EM map was placed into a pseudo P1 unit cell and converted to structure factors. The calculated map was further truncated within 3 Å around the TRPV2 model. Tight geometry constraints (secondary structure, hydrogen bonds, higher weight on ideal geometry) were used throughout the refinement in both real- and reciprocal-space refinements. A previously published cross-validation method was used to monitor overrefinement, and no significant separation was observed between FSCs of half maps against the refined model<sup>55</sup> (Supplementary Fig. 5). The MolProbity server (<http://molprobity.biochem.duke.edu/>) was used to guide the model refinement. The model contained amino acids 76–708 with several loops missing (194–203, 416–426, and 560–585), covering about 90% of the construct (Supplementary Fig. 1). Approximately 65% of side chains were built for the entire model, and the ARD and the C-terminal region were accountable for a substantial portion of missing side chains (>55%) because the electron density map in these regions were not well defined. The local CCs were calculated with Phenix with the reciprocal-space reflections (filtered at 4 Å) and the docked cholesterol molecules with their B factors matching the neighboring protein atoms<sup>53</sup>. For all structural alignments, the following range of residues was used: TRPV1, Val583–Ala594 and Ser629–Leu664; and TRPV2, Val541–Ala552 and Ser590–Leu624.

**Electrophysiology.** HEK293T cells (ATCC) were transfected with rabbit TRPV2 cDNA mixed with EGFP with Lipofectamine 2000 (Invitrogen) at 6 µg of DNA in a 60 mm dish (1:1 ratio (w/w)). HEK293T cells, commonly used for functional characterization of TRP channels, were used for electrophysiology and calcium imaging. Cells tested negative for mycoplasma contamination. Cells were reseeded on 12-mm round glass coverslips (Warner Instruments) 1 d after transfection. Approximately 48 h after transfection, whole-cell recordings were performed on single isolated green cells identified under a fluorescence microscope at room temperature. Glass pipettes (Sutter Instrument Company) were prepared (3–4 MΩ) with a pipette puller P1000 (Sutter Instrument Company). Data were acquired with an Axopatch 200B amplifier controlled by a Clampex 10 via a Digidata 1440A data-acquisition system (Axon Instruments). Currents were sampled at a rate of 10 kHz and filtered at 3 kHz. The pipette solution

contained 150 mM NaCl, 3 mM MgCl<sub>2</sub>, 5 mM EGTA and 10 mM HEPES, adjusted to pH 7.2, and bath solution containing 150 mM NaCl, 6 mM CsCl, 1.5 mM CaCl<sub>2</sub>, 1 mM MgCl<sub>2</sub>, 10 mM glucose and 10 mM HEPES, adjusted to pH 7.4.

**Calcium imaging.** Wild-type rabbit TRPV2 and the truncated TRPV2 construct were expressed in HEK293T cells (ATCC). HEK293T cells were plated on glass coverslips and transiently transfected with a mixture of DNA, Opti-MEM and FuGENE (Promega) according to the manufacturer's manual. Cells were seeded at 60 × 10<sup>3</sup> per well in the presence of 10 µM ruthenium red and incubated for 48 h at 37 °C. The transfected cells were washed in Hank's buffer and incubated with 2 µM Fura-2 AM in the presence of pluronic acid (Invitrogen) for 30–60 min. Imaging was performed as previously described<sup>56</sup>. In brief, frames were recorded every second at 340 nm and 380 nm, and the data were analyzed with Nikon Elements software.

41. Suloway, C. *et al.* Automated molecular microscopy: the new Legion system. *J. Struct. Biol.* **151**, 41–60 (2005).
42. Lander, G.C. *et al.* Appion: an integrated, database-driven pipeline to facilitate EM image processing. *J. Struct. Biol.* **166**, 95–102 (2009).
43. Mindell, J.A. & Grigorieff, N. Accurate determination of local defocus and specimen tilt in electron microscopy. *J. Struct. Biol.* **142**, 334–347 (2003).
44. Voss, N.R., Yoshioka, C.K., Radermacher, M., Potter, C.S. & Carragher, B. DoG Picker and TiltPicker: software tools to facilitate particle selection in single particle electron microscopy. *J. Struct. Biol.* **166**, 205–213 (2009).
45. Ludtke, S.J., Baldwin, P.R. & Chiu, W. EMAN: semiautomated software for high-resolution single-particle reconstructions. *J. Struct. Biol.* **128**, 82–97 (1999).
46. Ogura, T., Iwasaki, K. & Sato, C. Topology representing network enables highly accurate classification of protein images taken by cryo electron-microscope without masking. *J. Struct. Biol.* **143**, 185–200 (2003).
47. Scheres, S.H. RELION: implementation of a Bayesian approach to cryo-EM structure determination. *J. Struct. Biol.* **180**, 519–530 (2012).
48. Li, X. *et al.* Electron counting and beam-induced motion correction enable near-atomic-resolution single-particle cryo-EM. *Nat. Methods* **10**, 584–590 (2013).
49. Roseman, A.M. FindEM: a fast, efficient program for automatic selection of particles from electron micrographs. *J. Struct. Biol.* **145**, 91–99 (2004).
50. Scheres, S.H. Beam-induced motion correction for sub-megadalton cryo-EM particles. *eLife* **3**, e03665 (2014).
51. Heymann, J.B. & Belnap, D.M. Bsoft: image processing and molecular modeling for electron microscopy. *J. Struct. Biol.* **157**, 3–18 (2007).
52. Emsley, P. & Cowtan, K. Coot: model-building tools for molecular graphics. *Acta Crystallogr. D Biol. Crystallogr.* **60**, 2126–2132 (2004).
53. Adams, P.D. *et al.* PHENIX: a comprehensive Python-based system for macromolecular structure solution. *Acta Crystallogr. D Biol. Crystallogr.* **66**, 213–221 (2010).
54. Brown, A. *et al.* Tools for macromolecular model building and refinement into electron cryo-microscopy reconstructions. *Acta Crystallogr. D Biol. Crystallogr.* **71**, 136–153 (2015).
55. Fernández, I.S., Bai, X.C., Murshudov, G., Scheres, S.H. & Ramakrishnan, V. Initiation of translation by cricket paralysis virus IRES requires its translocation in the ribosome. *Cell* **157**, 823–831 (2014).
56. Peier, A.M. *et al.* A TRP channel that senses cold stimuli and menthol. *Cell* **108**, 705–715 (2002).